PAPER

Gyrokinetic modelling of light to heavy impurity transport in tokamaks

View the article online for updates and enhancements.

Gyrokinetic modelling of light to heavy impurity transport in tokamaks

K. Lim[1],[*] ⓘ**, X. Garbet**[2] ⓘ**, Y. Sarazin**[2] ⓘ**, V. Grandgirard**[2]**, K. Obrejan**[2]**,
M. Lesur**[1] **and E. Gravier**[1] ⓘ

[1] Institut Jean Lamour (IJL), UMR 7198 CNRS—Université de Lorraine, 54000 Nancy, France
[2] CEA, IRFM, F-13108 Saint-Paul-Lèz-Durance, France

E-mail: kyungtak.lim@univ-lorraine.fr

CrossMark

Abstract

Impurity transport is numerically investigated for different types of impurity, such as helium (He), argon (Ar), and tungsten (W). Both turbulent and neoclassical transports are treated self-consistently using the full-f gyrokinetic software GYSELA. For a light impurity (He), the transport is mainly controlled by turbulence, while neoclassical transport is found to be dominant in the case of a heavy impurity (W). The impact of a poloidal asymmetry of the impurity density is also studied in detail and it is found to be strong in case of a high charge impurity, due to its Boltzmann-type response. Such strong asymmetry might lead to a core accumulation of heavy impurities by reducing the thermal screening factor of neoclassical transport. The two main contributions to neoclassical transport—Pfirsch–Schlüter (PS) flux and banana–plateau (BP) flux—are also studied. Depending on their mass (A) and charge (Z), the magnitudes of each flux are determined accordingly. Tungsten shows a strong PS flux compared to the other impurities, while BP flux is dominant in the case of argon. An analytical model including the effect of poloidal asymmetry is compared with the numerical simulation and a good agreement is found between them.

Keywords: gyrokinetic, impurity, transport

(Some figures may appear in colour only in the online journal)

1. Introduction

Understanding the transport of impurities in a fusion reactor has been one of the important issues over the last few decades. In particular, the central accumulation of heavy (high-Z) impurities is widely recognized as a paramount concern, since it might result in a complete extinction of the burning plasma by radiative loss, even at concentrations as low as $\sim 10^{-5}$ [1]. Moreover, inherent light impurities injected at the edge to mitigate the heat power on the divertor [2] or produced by fusion reactions can lead to a dilution of the D–T fuel by degrading fusion efficiency.

The main causes of impurity transport can usually be summarized using three classes: (i) magnetohydrodynamics (MHD) activities caused by a sawtooth crash [3], tearing modes [4] or edge-localized modes [5, 6] facilitated by a redis-tribution of impurities; (ii) dominant turbulent transport, especially for light impurities [7, 8] and (iii) neoclassical transport—especially in the presence of impurity density poloidal asymmetry—mostly for heavy impurities [9, 10]. A large number of existing studies have reported that a core accumulation of W has been observed in different tokamaks [11–13]. Hopefully, avoiding or delaying such accumulation can be accomplished by the application of an RF heating system, such as ion cyclotron resonance Heating (ICRH) or electron cyclotron resonance heating (ECRH), leading to a significant reduction of impurities in the core plasma [14–16]. However, discrepancies still exist between theoretical predictions and experimental data with respect to the density or temperature profile of impurities during tokamak discharges [8, 17].

In recent years, special attention has been paid to the poloidal asymmetry of impurity concentrations and its impact on impurity transport [18–23]. Unlike conventional

* Author to whom any correspondence should be addressed.

neoclassical prediction, which assumes an almost uniform impurity distribution over the flux surface [24], a strong poloidal asymmetry has repeatedly been observed in various cases and mounting evidence suggests that taking account of such asymmetry is key for a predictive model [9].

A linearized collision operator has successfully been implemented in the full-*f* gyrokinetic software GYSELA [25]. Since its first use for neoclassical transport, numerical improvements have been achieved, offering a better agreement with theoretical prediction. Using the collision operator in the gyrokinetic code enables the study of impurity transport in turbulent and collisional regimes at the same time. Taking these two channels into account simultaneously is of great interest to clarify the synergy effect that presumably originates from poloidal density asymmetry driven by turbulence [27].

In this work, as an extension of previous work [28], GYSELA numerical simulations are extended to investigate the impurity transport of various impurities in different collisional regimes, in particular, helium (He), argon (Ar), and tungsten (W) representing low, intermediate, and high collisional regimes, respectively. To achieve this end, turbulent and neoclassical transports in the presence of poloidal asymmetry driven by turbulence are compared with an analytical model in each case and the effects of poloidal asymmetry on neoclassical transport are alsoinvestigated.

This paper is organized as follows. In section 2, analytical models for impurity transport are derived for the case of non-uniform density distribution. Section 3 outlines the overall numerical results of comparing the turbulent and neoclassical particle flux of each species with impurity poloidal asymmetry due to turbulence and the impact of the non-uniform distribution of impurity density on impurity transport is also described in detail. Conclusions are drawn in the final section and some suggestions for future work are proposed.

2. Neoclassical impurity flux

In this section, an analytical description of neoclassical impurity flux is derived using two different assumptions. First, neoclassical fluxes are expressed as a function of the chewgoldberger-low (CGL)-pressure tensor [29], assuming weak poloidal asymmetries of the impurity density. The purpose of such derivation is to clarify the main driving terms of the neoclassical fluxes i.e. banana–plateau (BP) and Pfirsch–Schlüter (PS). Second, a more detailed form of impurity flux is given, including the analytic impact of the poloidal asymmetries of the density, the effects of which are significant compared to neoclassical particle fluxes, changing an order of magnitude or even the sign [18]. This analytical formula will be used for a later comparison with numerical simulations in section 3. A more detailed derivation of the latter can be found in [28].

2.1. Impurity flux with a uniform density distribution

The analytical form for a neoclassical impurity flux can be derived from the gyrokinetic equation.

$$\frac{\partial \bar{F}_z}{\partial t} + \frac{1}{B_\parallel^*} \nabla_z \cdot \left(\dot{\boldsymbol{z}} B_\parallel^* \bar{F}_z \right) = \mathcal{C}(\bar{F}_z), \tag{1}$$

where $\bar{F}_z$ is the distribution function of the impurity and $B_\parallel^* = B + \frac{m_z}{eZ} v_\parallel \mathbf{b} \cdot (\nabla \times \mathbf{b})$ is the volume element in guiding-center velocity space and $\mathcal{C}$ is the collision operator. Here, the difference in trajectory between the cyclotron's motion and the guiding center is compensated for by investigating the drift kinetic limit of large scale flows, where details of the short-scale gyrations are suppressed.

In the steady state, the conservative form of particle flux $\nabla \cdot \boldsymbol{\Gamma} = 0$ can be obtained by taking the first moment of equation (1) where $\boldsymbol{\Gamma} = \Gamma_\parallel \mathbf{b} + \boldsymbol{\Gamma}_\perp$. The perpendicular flow can then be recast as:

$$\boldsymbol{\Gamma}_{\perp \mathbf{z}} = \boldsymbol{\Gamma}_\mathrm{E} + \boldsymbol{\Gamma}_\mathrm{D} + \boldsymbol{\Gamma}_\mathrm{mag} = N_z \boldsymbol{v}_\mathrm{E} + N_z \langle \boldsymbol{v}_{\mathrm{D}z} \rangle - \nabla \times \left[N_z \left\langle \frac{\mu}{Ze} \mathbf{b} \right\rangle \right], \tag{2}$$

where $\boldsymbol{v}_\mathrm{E}$ is the $E \times B$ drift and $\boldsymbol{v}_\mathrm{D}$ is the magnetic drift. The magnetization flux $\Gamma_\mathrm{mag} = \nabla \times \mathcal{M}_z$ with $\mathcal{M}_z = - \int \mathrm{d}^3 v \bar{F}_z \mu \boldsymbol{b}$ is added to account for the correction associated with the cyclotron's motion of particles around its guiding centre [30] and the bracket is an average over the distribution function.

$$\langle \ldots \rangle = \frac{1}{N} \int \mathrm{d}^3 \boldsymbol{v} \bar{F}_z \ldots . \tag{3}$$

Applying an average of the distribution function over the magnetic drift $\boldsymbol{v}_\mathrm{D}$ leads to the impurity flux as a function of the CGL-pressure tensor. After properly arranging all the terms in equation (2), one can find an analytical expression of the neoclassical particle BP and PS fluxes (appendix A).

$$\langle \boldsymbol{\Gamma}_\mathrm{BP} \cdot \nabla \psi \rangle_\psi = - \frac{I}{Ze} \frac{\langle \boldsymbol{B} \cdot \nabla \cdot \boldsymbol{\Pi} \rangle_\psi}{\langle B^2 \rangle_\psi} \tag{4}$$

$$\langle \boldsymbol{\Gamma}_\mathrm{PS} \cdot \nabla \psi \rangle_\psi = - \frac{I}{Ze} \left\langle (N e \mathbf{b} \cdot \nabla \phi + \mathbf{b} \cdot \nabla \cdot \boldsymbol{\Pi}) \right. \\ \left. \times \left(\frac{1}{B} - \frac{B}{\langle B^2 \rangle_\psi} \right) \right\rangle_\psi, \tag{5}$$

where $I = R B_\varphi$ is related to the poloidal current that flows through a magnetic surface, $\boldsymbol{\Pi}$ is the CGL-pressure tensor and the bracket $\langle \ldots \rangle_\psi$ corresponds to a flux surface average.

The BP flux, which is dominant in the long mean-free-path regime, is mainly driven by pressure anisotropy. The origin of pressure anisotropy is usually due to the magnetic drift driven by a non-uniform magnetic field. Since the effect of collisions is less strong than that of advection in this regime, pressure is not completely isotropized, leading to perpendicular flux [24]. Conversely, the main driving source of PS flux arises from poloidal variation of the friction force [24]. In this regime, the contribution of pressure anisotropy vanishes because of strong collisions.

2.2. Impurity flux with poloidal asymmetries

2.2.1. Determination of the poloidal variation of impurity flux Γ_z.
In what follows, we derive neoclassical impurity flux in presence of poloidal density asymmetry. As it is already treated in the previous section, the total impurity flux from the

gyrokinetic equation can be written

$$\mathbf{\Gamma}_z = \Gamma_{\|z}\mathbf{b} + N_z\frac{\boldsymbol{B}}{B^2} \times \nabla\phi + \frac{\boldsymbol{B}}{ZeB^2} \times \nabla \cdot \mathbf{\Pi}. \quad (6)$$

Using an axisymmetric notation

$$\nabla\phi = \frac{\partial\phi}{\partial\psi}\nabla\psi + \frac{\partial\phi}{\partial\theta}\nabla\theta$$

$$\nabla P_{\perp z} = \frac{\partial P_{\perp z}}{\partial\psi}\nabla\psi + \frac{\nabla P_{\perp z}}{\partial\theta}\nabla\theta \quad (7)$$

equation (6) can be reformulated as follows:

$$\mathbf{\Gamma}_z = \mathrm{K}_z\boldsymbol{B} - N_z\Omega_z R^2\nabla\varphi + \frac{\Pi_{\|z}}{ZeB}(\mathbf{b} \times \boldsymbol{\kappa})$$
$$+ \left(N_z\frac{\partial\phi}{\partial\theta} + \frac{1}{Ze}\frac{\partial P_{\perp,z}}{\partial\theta}\right)\frac{\mathbf{b}}{B} \times \nabla\theta, \quad (8)$$

where $\Pi_{\|z} = P_{\|z} - P_{\perp z}$ is the pressure anisotropy, $\boldsymbol{\kappa} = -\mathbf{b} \times (\nabla \times \boldsymbol{b})$ is the magnetic curvature and we have introduced the following relations:

$$\Omega_z = \frac{\partial\phi}{\partial\psi} + \frac{1}{N_zZe}\frac{\partial P_{\perp z}}{\partial\psi}$$

$$\mathrm{K}_z = \frac{\Gamma_{\|z}}{B} + \frac{I}{B^2}N_z\Omega_z. \quad (9)$$

In the above equation, $K_z(\psi, \theta)$ is a function of the poloidal angle and a more precise form of it can be obtained using the incompressibility of impurity flow $\nabla \cdot \Gamma_z = 0$. The detailed derivation used to find $K_z(\psi, \theta)$ is described in [28] and we will use the value of $K_z = K_{z0}(\psi) + K_{z1}(\psi, \theta)$ directly from the aforementioned paper.

$$K_{z0}(\psi) = \langle K_z\rangle_\psi$$

$$K_{z1}(\psi, \theta) = -\frac{1}{B}\frac{\partial}{\partial\psi}\left(\frac{I\Pi_{\|z}}{ZeB}\right) + \left\langle\frac{1}{B}\frac{\partial}{\partial\psi}\left(\frac{I\Pi_{\|z}}{ZeB}\right)\right\rangle. \quad (10)$$

2.2.2. Link between the frictional force $\mathcal{F}$ and K_z. The analytical form of the neoclassical impurity flux can be also derived from the momentum equation by taking its toroidal projection:

$$mN\frac{\partial\boldsymbol{V}}{\partial t} + \nabla \cdot \mathbf{\Pi} - eN(\boldsymbol{E} + \boldsymbol{V} \times \boldsymbol{B}) = \mathcal{F}, \quad (11)$$

where the stress tensor $\mathbf{\Pi} = \boldsymbol{P} + mN\boldsymbol{V}\boldsymbol{V}$ and $\mathcal{F} = \int m\boldsymbol{v}\mathcal{C}(f)\mathrm{d}^3v$ is the frictional force.

By projecting the above equation in the $R\hat{\varphi}$-direction and applying the flux surface average, we can rewrite the above equation as follows:

$$\left\langle R\hat{\varphi} \cdot \frac{\partial(m_zN_z\boldsymbol{V}_z)}{\partial t}\right\rangle + \langle R\hat{\varphi} \cdot \nabla \cdot \mathbf{\Pi}\rangle$$
$$- \langle N_zZeR\hat{\varphi} \cdot (\boldsymbol{E} + \boldsymbol{V} \times \boldsymbol{B})\rangle = \langle R\mathcal{F}_{\|zi}\rangle. \quad (12)$$

Neoclassical theory usually assumes a steady state ($\partial_t = 0$) and a toroidal axisymmetry ($\partial_\varphi = 0$). Also, the stress tensor $\mathbf{\Pi}$ is a small term in neoclassical ordering, compared to other components in the case of strong collisions, thus it is

often neglected. Using the relation $\boldsymbol{B} = I(\psi)\nabla\varphi + \nabla\varphi \times \nabla\psi$ where I is related to the plasma current and $\hat{\varphi} = R\nabla\varphi$, the particle flux across magnetic surfaces can be derived as follows [31] (the detailed expression of $\mathcal{F}_{\|zi}$ is explained in appendix C):

$$\langle\Gamma_z \cdot \nabla\psi\rangle^{\mathrm{neo}} = -\left\langle\frac{I\mathcal{F}_{\|zi}}{ZeB}\right\rangle. \quad (13)$$

2.2.3. Impurity flux with poloidal asymmetries. Finally, one can find the analytical form of the impurity flux with poloidal asymmetry by properly arranging equations (10), (13), and (C.2). As already shown in the previous section, one can divide the total impurity flux into two different channels $\Gamma_{\mathrm{neo}}^\psi = \Gamma_{\mathrm{BP}}^\psi + \Gamma_{\mathrm{PS}}^\psi$.

$$\Gamma_{\mathrm{BP}} = -\frac{I}{Ze}\left\langle\frac{B^2}{N_z}\right\rangle_\psi^{-1}$$
$$\times \left\langle\frac{\boldsymbol{B}\cdot\nabla\theta}{N_z}\left[\frac{\partial P_{\perp z}}{\partial\theta} + B\frac{\partial}{\partial\theta}\left(\frac{\Pi_{\|z}}{B}\right)\right]\right\rangle_\psi \quad (14)$$

$$\Gamma_{\mathrm{PS}} = \frac{I}{Ze}m_z\nu_{zi}\left\{\frac{T_i}{e}\frac{I}{L_{\psi,i}}\left(\left\langle\frac{N_z}{B^2}\right\rangle_\psi - \left\langle\frac{B^2}{N_z}\right\rangle_\psi^{-1}\right)\right.$$
$$- u\left(\langle N_z\rangle_\psi - \frac{\langle B^2\rangle_\psi}{\left\langle\frac{B^2}{N_z}\right\rangle_\psi}\right) + \frac{T_iI}{e}\left(\left\langle\frac{N_z}{B^2L_{\psi,z}}\right\rangle_\psi\right.$$
$$- \left\langle\frac{1}{L_{\psi,z}}\right\rangle_\psi\left\langle\frac{B^2}{N_z}\right\rangle_\psi^{-1}\right) - \left\langle\frac{1}{B}\frac{\partial}{\partial\psi}\left(\frac{I\Pi_{\|z}}{ZeB}\right)\right\rangle_\psi$$
$$\left.+ \frac{\left\langle\frac{B}{N_z}\frac{\partial}{\partial\psi}\left(\frac{I\Pi_{\|z}}{ZeB}\right)\right\rangle_\psi}{\left\langle\frac{B^2}{N_z}\right\rangle_\psi}\right\}, \quad (15)$$

where $1/L_\psi = 1/L_{\psi i} + 1/L_{\psi z}$ with $1/L_{\psi\,i} = \partial_\psi \ln P_i - \frac{3}{2}\partial_\psi \ln T_i$ and $1/L_{\psi z} = -\frac{1}{T_iZN_z}\partial_\psi P_{\perp z}$ and u is the value related to the poloidal velocity of the main ion.

In the trace limit of impurities ($N_zZ^2/N_i) \ll 1$, u can be expressed as

$$u = \left(k_{\mathrm{neo}} - \frac{3}{2}\right)\frac{If_{\mathrm{c}}}{e\langle B^2\rangle_\psi}, \quad (16)$$

where the value of $k_{\mathrm{neo}} \approx 1.17$ is obtained in the limit of a large aspect ratio $\epsilon \ll 1$ with the main ion in the banana regime [32]. Thus, the following formula $u \approx -0.33\frac{If_{\mathrm{c}}}{e\langle B^2\rangle_\psi}$ will be used for further analysis. Here, f_{c} represents the fraction of circulating particles and can be obtained in a large aspect ratio with a circular cross-section

$$f_{\mathrm{c}} = 1 - f_t = \frac{3\langle B^2\rangle_\psi}{4}\int_0^{\lambda_{\mathrm{c}}}\frac{\mathrm{d}\lambda}{\langle\sqrt{1 - \lambda B}\rangle_\psi} \approx 1 - 1.46\sqrt{\epsilon}, \quad (17)$$

where $\lambda = \mu/E$ is the pitch angle and $\lambda_{\mathrm{c}} = B_{\max}^{-1}$ is the critical λ for trapping.

Comparing equations (4) and (5) with equations (14) and (15) shows how unevenly distributed impurities impose a considerable effect on their fluxes. Note that the main driving sources for BP/PS fluxes—pressure anisotropy for the BP flux and a poloidal variation of frictional force for the PS flux—are unchanged, while additional terms have been added in equation (15) arising from the poloidal dependency of $K_{z1}(\psi, \theta)$ in equation (10). The presence of the $\Pi_{\|z}$ term in equation (15) may seem odd at first sight, since pressure tend to be isotropic in the highly collisional regime. However, it has been pointed out that even in the high collisional regime, pressure anisotropy can still have an influence on a PS flux [28].

3. Numerical results

Different kinds of impurity coexist during a plasma discharge. Depending on its mass (A) and charge (Z), the main impurity flux can accordingly be determined, whether turbulent or neoclassical. Thus, the purpose of this section is, first of all, to provide the impurity flux of different species in the presence of poloidal asymmetries generated by turbulence and to compare them with the analytical models discussed previously. Second, the effect of poloidal asymmetries on impurity transport is investigated in detail. To achieve this end, we selected three impurities—helium ($Z = 2$, $A = 4$), argon ($Z = 18$, $A = 40$) and tungsten ($Z = 40$, $A = 184$)—each representing different collisional regimes according to the normalized collisionality ν_a^* [24]:

$$\nu_a^* = \frac{\nu_{\text{detrap},a}}{\omega_{b,a}} \approx \frac{qR_0}{\epsilon^{3/2}} \frac{\nu_a}{v_{Ta}} \tag{18}$$

$$= \frac{qR_0}{\epsilon^{3/2}} \frac{4\sqrt{\pi}}{3} \frac{e^4 \ln \Lambda}{(4\pi\epsilon_0)^2} \frac{Z_a^2}{T_a^2}$$

$$\times \left[n_a Z_a^2 + \sum_{b \neq a} \sqrt{2} n_b Z_b^2 \frac{\left(1 + \frac{m_a}{m_b}\right)}{\left(1 + \frac{v_{Tb}^2}{v_{Ta}^2}\right)^{3/2}} \right]. \tag{19}$$

While the main ions are in the banana regime with $\nu_D^* = 0.1$ at mid radius, the relative ratio of the detrapping frequency $\nu_{\text{detrap},a} = \nu_a/2\epsilon$ versus the bounce frequency $\omega_{b,a} = \frac{v_{Ta}\sqrt{\epsilon}}{\sqrt{2}\pi qR}$ determines three collisional regimes: $\nu^* \ll 1$ for the banana regime, $1 \ll \nu^* \ll \epsilon^{-3/2}$ for the plateau regime and $\nu^* \gg \epsilon^{-3/2}$ for the PS regime (figure 1).

For numerical simulations, the following parameters in table 1 are chosen for impurities. With a given density and temperature profile for the main ions ($R/L_{ni} = 2.2$ and $R/L_{Ti} = 6$), the main instability is basically the ion temperature gradient instability and electrons are treated adiabatically. An isotropic heat source is added close to the inner boundary of simulations [33], allowing convergence toward the steady state. In addition, a Krook operator is applied at the outer boundary region for artificial damping of the heat flux. Without any further 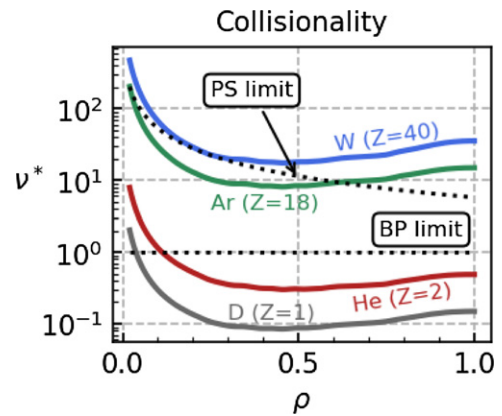assumptions of ionization or recombination, the impurity concentration is kept at the trace limit ($\mathcal{C}_z = 10^{-6}$) so that the background turbulence is not affected by the presence of impurities. Also, all numerical simulations are performed in axisymmetric geometry with concentric magnetic surfaces. The magnetic field is defined as $\boldsymbol{B} = (B_0 R_0/R)[\frac{r}{q(r)R_0}\boldsymbol{e}_\theta + \boldsymbol{e}_\varphi]$, where B_0 is the magnetic field at the axis and the safety profile is given by $q(r) = 1.5 + 1.3 \exp\left(2.5 \log\left(\frac{r}{a}\right)\right)$.

Although electrons are treated adiabatically, running a simulation with an impurity requires considerable computation time, since a higher resolution is necessary for the impurity Larmor radius ($\rho_z = \frac{1}{Z}\sqrt{\frac{m_z}{m_i}}\rho_i$). To overcome this issue, the same strategy is applied as that used in [28] has been applied: (i) the first simulation runs without impurity until turbulence is well developed and steady. At this stage, the numerical grid $(N_r, N_\theta, N_\varphi, N_{v_\parallel}, N_\mu) = (256, 512, 32, 127, 64)$ is used for the main ions. (ii) Once the main ions reach a steady state, the high-resolution numerical grid $(N_r, N_\theta, N_\varphi, N_{v_\parallel}, N_\mu) = (512, 1024, 32, 127, 64)$ is used without the impurity in order to reorganize the system before adding the impurity. (iii) After the reorganization, the impurity is added to the simulation with the same numerical grid as the previous step.

The duration of each simulation is close to the ion confinement time, and the final stage (iii) of each impurity lasts for a sufficiently long time. However, the confinement time required for impurities to reach the steady state is much longer than the ion confinement time, hence the radial plasma profiles of the impurities, such as density and temperature, are not completely steady.
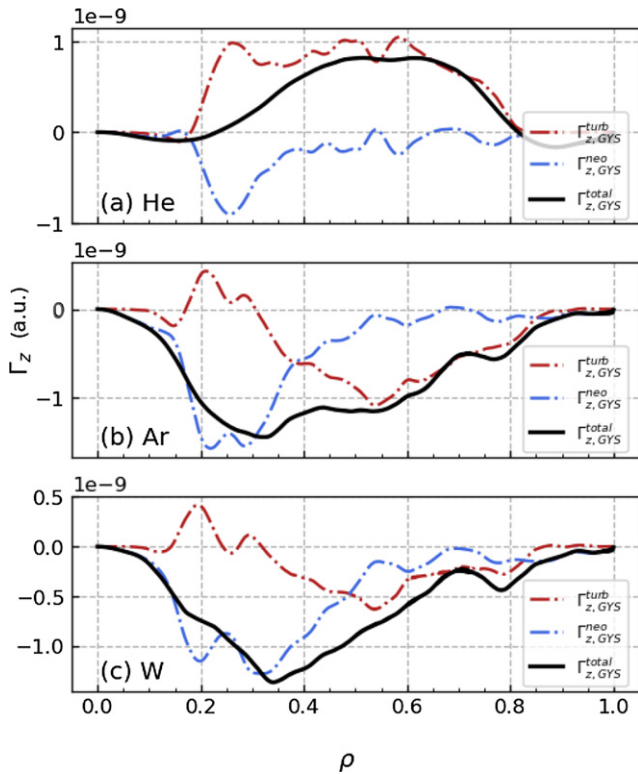

Figure 1. Radial profile of collisionality for D, He, Ar and W.

Table 1. Numerical simulation parameters.

Parameter	Normalization
Time step	$\Delta t \omega_{ci} = 16$
Normalized gyroradius	$\rho_* = \rho_i/a = 1/190$
Impurity concentration	$\mathcal{C}_z = 10^{-6}$
Inverse aspect ratio	$\epsilon = R_0/a = 4.4$
Density	$R/L_n = 2.2$
Temperature	$R/L_T = 6$
Magnetic field	$\boldsymbol{B} = \left(\frac{B_0 R_0}{R}\right)\left[\frac{r}{q(r)R_0}\boldsymbol{e}_\theta + \boldsymbol{e}_\varphi\right]$
Safety factor	$q(r) = 1.5 + 1.3 \exp[2.5 \log(r/a)]$

Figure 2. Impurity fluxes of different impurities in the presence of poloidal asymmetries, obtained by numerical simulation (GYSELA). Total impurity flux (black solid line) is separated into a turbulent part (red dashed line) and a neoclassical part (blue dashed line).

3.1. Impurity flux with poloidal asymmetry driven by turbulence

By convention, the total impurity flux can be expressed as the sum of two different contributions $\Gamma_{tot} = \Gamma_{turb} + \Gamma_{neo}$. Various approaches have been suggested to define such fluxes properly [27]. In this work, we adopt the following definitions:

$$\langle \Gamma_z^{turb} \cdot \nabla \psi \rangle_\psi = \left\langle \int d^3 v \bar{F}_z \overline{v}_E^{n \neq 0} \cdot \nabla \psi \right\rangle_\psi \qquad (20)$$

$$\langle \Gamma_z^{neo} \cdot \nabla \psi \rangle_\psi = \left\langle \int d^3 v \bar{F}_z (v_{D,s} + \overline{v}_E^{n=0}) \cdot \nabla \psi \right\rangle_\psi, \qquad (21)$$

where n is the toroidal mode number.

The impurity fluxes, averaged out over $4000 \omega_{ci}$, are shown respectively in figure 2, where the black solid line stands for the GYSELA numerical flux which is the sum of the turbulent flux (red dashes) and the neoclassical flux (blue dashes).

A distinct difference between species is clearly observed in figure 2. For helium, the dominant flux mainly originates from turbulent transport flowing outward from the core (positive Γ_z) except in the region $\rho \sim 0.3$, where an overestimation of the neoclassical flux is presumably produced by poloidal density asymmetry. These results fit well with our prior expectation that helium, as a light impurity, is placed in the banana regime (figure 1) where collisional effects are small compared

to those of turbulent fluxes. Also, the outward flow of an impurity usually gives rise to a hollow density profile (figure 3). In recent works [17, 34], such hollow profiles were experimentally observed in the ASDEX Upgrade and JET tokamaks with neutral beam injection (NBI) heating plasmas (peaked density profiles of helium have also been reported in the case of high-ECRH systems).

The neoclassical contribution to the total impurity flux becomes larger when impurities with higher Z are considered: in the simulations we have performed, it is significant for argon and tungsten. Argon, whose collisionality is mostly extends mostly over the plateau region (figure 1), shows two distinct regions where the total flux (black solid line) is roughly aligned (i) with neoclassical flux ($\rho < 0.3$) and (ii) with turbulent flux ($\rho > 0.5$). In terms of magnitude, turbulent flux is comparable to neoclassical flux, giving a nearly equal contribution to the total flux. Unlike helium, argon generates a inward flux (Γ_z negative) leading to accumulation in the core (figure 3).

For tungsten, the heaviest of the analyzed impurities, turbulent flux is largely reduced, while neoclassical transport still exerts an important effect in the core. The overall impurity flux is directed inward, driving its core accumulation due to neoclassical convection (figure 3). A large number of experimental cases have already confirmed core accumulation [11–13] and recent studies have proposed that the appropriate use of an additional heating system might mitigate such accumulation by reducing neoclassical convection and increasing turbulent diffusion [18, 35]. In this work, no additional heating systems are used except the heat source for flux-driven simulations.

A comparison of the neoclassical part of numerical flux (blue dashes) and that obtained from the analytical model (grey solid) using equations (14), and (15) is depicted in figure 4. At this point, special attention has to be paid to how our analytical formula is numerically calculated. Unlike other models which use a solution of the drift-kinetic equation (NEO [36]) or a moment approach (NCLASS [24, 37]), GYSELA makes direct use of numerical data to estimate the neoclassical flux, which means every term in equations (14), and (15) is calculated at each time step to predict the neoclassical transport.

It is clearly shown in figure 4 that in all impurity cases, our numerical simulations reproduce satisfying results in conjunction with our analytical model. The neoclassical flux is directed inward for all impurities due to the inward neoclassical convection driven by the main ion density profile. In agreement with our previous results, helium generates a weak neoclassical flux compared to other impurities. It would be also instructive to analyze the neoclassical flux in detail using its components.

In figure 5, the radial BP and PS fluxes are calculated from GYSELA numerical simulations using the analytical formula equations (14) and (15). As expected, tungsten produces the most important PS flux compared to the other impurities, due to its high collisionality, while the PS flux due to helium is almost negligible. For BP fluxes, argon, whose collisionality extends over the plateau region, produces a stronger BP flux than the other species. Moreover, in the banana regime, helium starts to generate a BP flux.
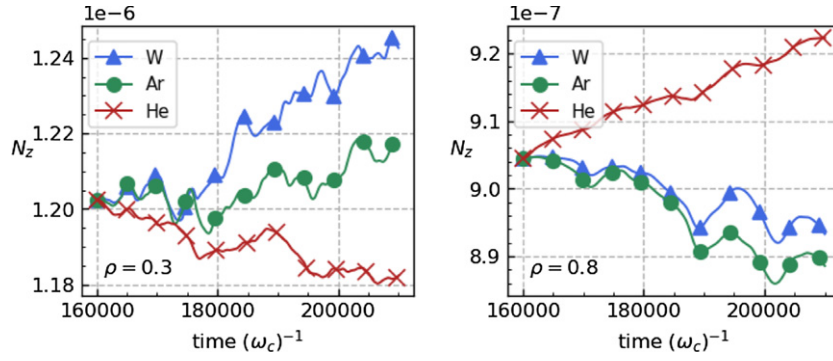
Figure 3. Time evolution of impurity density in the core (left) and at the edge (right).
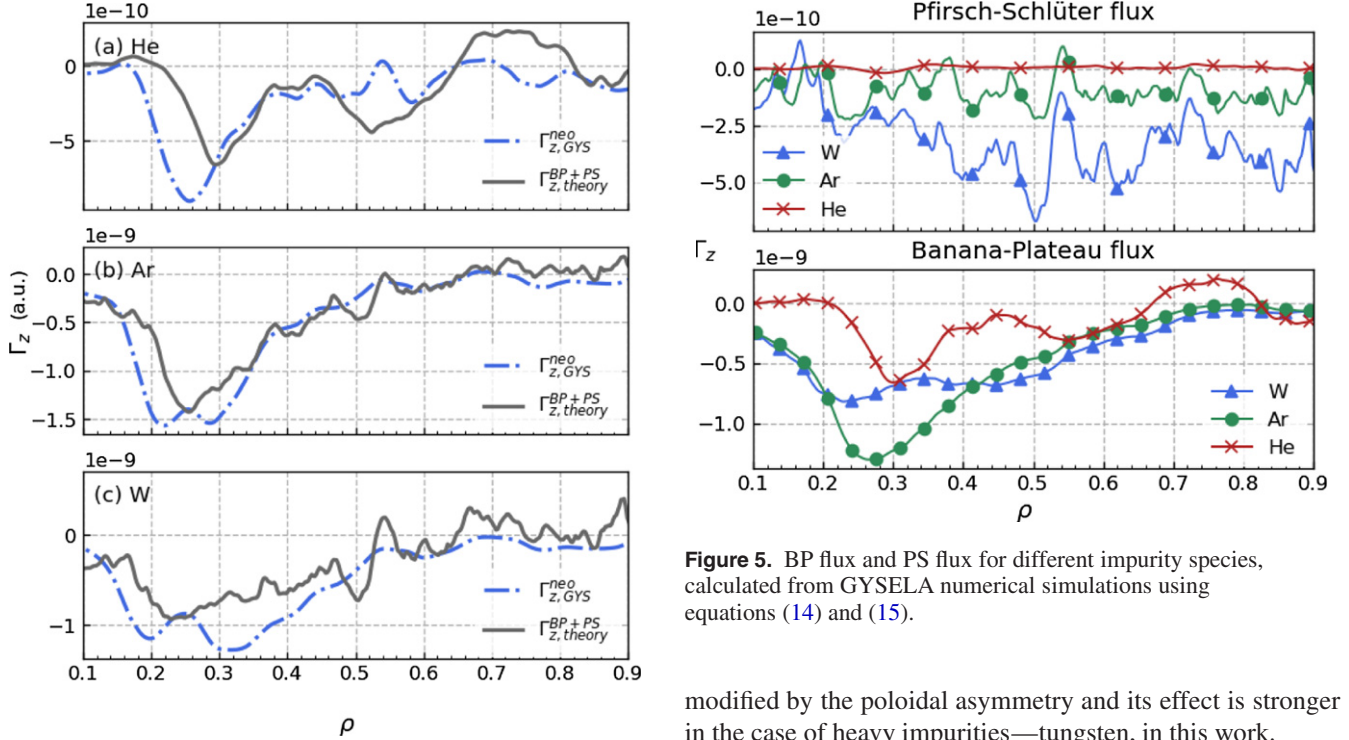

Figure 4. Comparison between the neoclassical flux obtained by numerical simulation ((GYSELA) (blue dashed line) from equation (21) and that obtained from the analytical model (grey solid line) using equations (14) and (15).

Figure 5. BP flux and PS flux for different impurity species, calculated from GYSELA numerical simulations using equations (14) and (15).

3.2. Poloidal asymmetry driven by background turbulence

A number of studies have pointed out that a non-uniform distribution of impurity over the flux surfaces can strongly modify neoclassical transport [19, 32, 38] while its contribution to turbulent transport seems less significant [9]. Although there are many factors that can trigger poloidal asymmetry, in this paper we restrict ourselves to poloidal asymmetry driven by turbulence only.

The poloidal asymmetries generated by turbulence are expected to be larger for a high-Z impurity since it has a Boltzmann-type response to electric potential, thus its response is proportional to the impurity charge. According to equation (15), PS flux is mostly driven by the poloidal variation of frictional force which is a function of the impurity density N_z from equation (C.2). Therefore, it is clear that the PS flux is

modified by the poloidal asymmetry and its effect is stronger in the case of heavy impurities—tungsten, in this work.

This fact is clearly shown in figure 6, in which the perturbed densities $\tilde{N}_z = \frac{N_z - \langle N_z \rangle_\psi}{\langle N_z \rangle_\psi}$ of different impurities are presented in the poloidal section. As expected, tungsten shows the strongest poloidal asymmetry ($\sim 20\%$), while helium presents a very weak asymmetry ($\sim 3\%$). Such an asymmetry of impurity density can be expressed as $N_z(\psi, \theta) = N_z(\psi)[1 + \delta \cos \theta + \Delta \sin \theta]$, where δ and Δ represent '*in–out*' and '*up–down*' asymmetries, respectively. According to [18], it is usually an '*in–out*' asymmetry that plays an important role in neoclassical transport, since the geometric factor in equation (15) (corresponding to P_A, P_B in equation (23)) can be recast as a function of δ and Δ and the '*up–down*' asymmetry Δ only appears as a second-order term in the impurity flux

$$\frac{\langle B^2 \rangle_\psi}{\langle N_z \rangle_\psi} \left[\left\langle \frac{N_z}{B^2} \right\rangle_\psi - \left\langle \frac{B^2}{N_z} \right\rangle_\psi^{-1} \right] = 2\epsilon(\epsilon + \delta) + \frac{\delta^2 + \Delta^2}{2}$$

$$\frac{\langle B^2 \rangle_\psi}{\langle N_z \rangle_\psi} \left[\frac{\langle N_z \rangle_\psi}{\langle B^2 \rangle_\psi} - \left\langle \frac{B^2}{N_z} \right\rangle_\psi^{-1} \right] = \epsilon \delta + \frac{\delta^2 + \Delta^2}{2}.$$
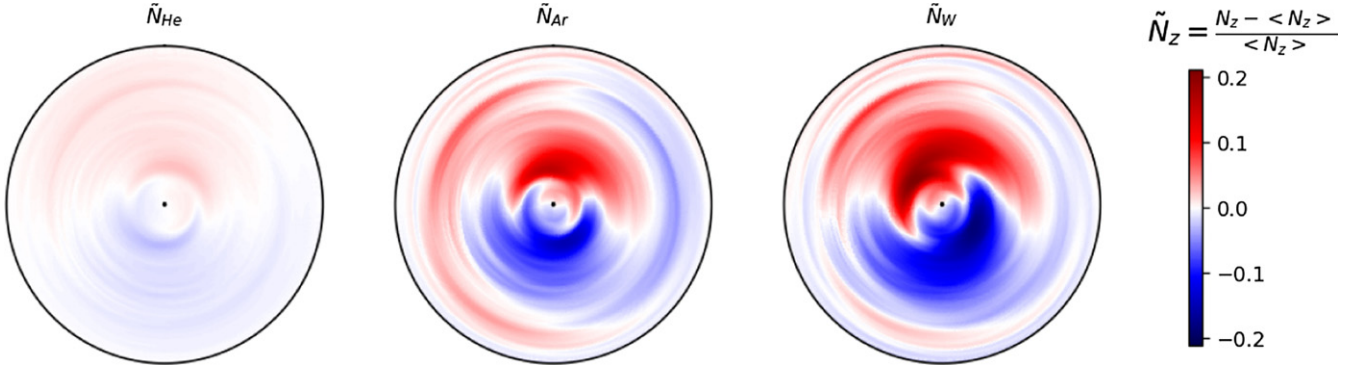
$$(22)$$

Figure 6. Poloidal asymmetries of impurity density given by numerical simulations performed using GYSELA.
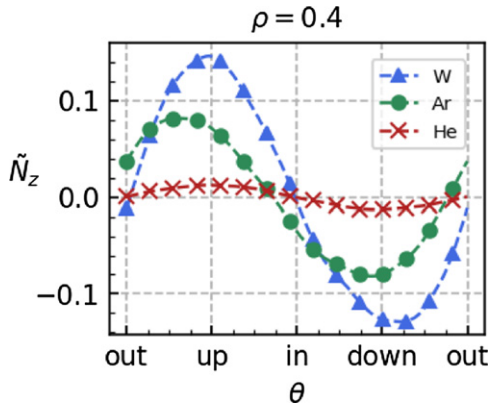

Figure 7. Impurity density distribution as a function of the poloidal angle given by the GYSELA numerical simulations.

However, poloidal asymmetry driven by turbulence tends to generate an '*up–down*' asymmetry (figure 7) through the poloidal convective cells [39]. Such an '*up–down*' asymmetry is less dramatic than neoclassical '*in–out*' asymmetries and its different impact has already been treated in [32].

Poloidal asymmetry affects neoclassical transport, but it can also change the so-called *thermal screening factor* H_{neo}. As the name suggests, this term, related to the main ion temperature profile L_{Ti}, prevents impurities from accumulating in the core. Derived from the main ion parallel heat flux in neoclassical theory, the factor is usually equal to $H_{\mathrm{neo}} \simeq -\frac{1}{2}$ when the main ions are in the banana regime [24], but this screening term is also susceptible to modification by poloidal asymmetry. To clarify this mechanism, it is helpful to rewrite equation (15) in a different way, as was done in [19]:

$$
\begin{aligned}
R\langle \Gamma_Z^{\mathrm{neo}} \cdot \nabla \psi \rangle_\psi &\propto \left[-\frac{R}{L_{ni}} - H_{\mathrm{neo}} \frac{R}{L_{Ti}} + \frac{1}{Z} \frac{R}{L_{nz}} \right] \\
&\propto \left[\left(-\frac{R}{L_{ni}} - H_{\mathrm{sym}} \frac{R}{L_{Ti}} + \frac{1}{Z} \frac{R}{L_{nz}} \right) P_A \right. \\
&\quad \left. - 0.33 P_B f_c \frac{R}{L_{Ti}} \right],
\end{aligned}
\tag{23}
$$

where $H_{\mathrm{neo}} = H_{\mathrm{sym}} + 0.33 \frac{P_B}{P_A} f_c$ with the factor $H_{\mathrm{sym}} = -\frac{1}{2}$ in the absence of poloidal asymmetries. This factor appears in the expression of $\frac{1}{\tilde{L}_{\psi,i}} = \frac{\partial \ln \tilde{N}_i}{\partial \psi} + H_{\mathrm{sym}} \frac{\partial \ln T_i}{\partial \psi}$ in equation (15).

In this equation, the second term corresponds to the thermal screening term and f_c is the fraction of passing particles. The geometric factors P_A, P_B quantify the impact of poloidal asymmetry, defined as follows:

$$
\begin{aligned}
P_A &= \frac{1}{2\epsilon^2} \frac{\langle B^2 \rangle_\psi}{\langle N_z \rangle_\psi} \left[\left\langle \frac{N_z}{B^2} \right\rangle_\psi - \left\langle \frac{B^2}{N_z} \right\rangle_\psi^{-1} \right] \\
P_B &= \frac{1}{2\epsilon^2} \frac{\langle B^2 \rangle_\psi}{\langle N_z \rangle_\psi} \left[\frac{\langle N_z \rangle_\psi}{\langle B^2 \rangle_\psi} - \left\langle \frac{B^2}{N_z} \right\rangle_\psi^{-1} \right].
\end{aligned}
\tag{24}
$$

Equation (23) reveals that a non-uniform distribution of impurities can modify the neoclassical flux or even reduce the temperature screening term by facilitating the accumulation of impurities at the core. From equation (24), it readily appears that if the impurity density is uniform over the flux surfaces, i.e. if $\langle N_z \rangle = N_z$, then $P_A = 1$ and $P_B = 0$. In this case, standard neoclassical results are recovered. The radial profiles of P_A, P_B for different impurities are presented in figure 8, where the outer regions $\rho < 0.1$ and $\rho > 0.9$ are excluded to avoid the effects of boundary conditions. Although external heating systems are absent in our cases, background turbulence generates a poloidal asymmetry of density and it is strongly enhanced for W due to its high charge and large mass.

The impact of poloidal asymmetry on thermal screening is depicted on figure 9. The theoretical prediction of neoclassical fluxes in two different cases: (i) with thermal screening $H_{\mathrm{sym}} = -\frac{1}{2}$ (red solid line) and (ii) without thermal screening $H_{\mathrm{sym}} = 0$ (green solid line) are compared with the neoclassical flux obtained from the GYSELA simulation (blue dashed line). The effect of H_{sym} on impurity transport can easily be understood by looking at the relative magnitude of each flux. When the thermal screening effect is removed, i.e., $H_{\mathrm{sym}} = 0$, the neoclassical flux shows a strong inward flux, leading to strong core accumulation, while the accumulation is mitigated in the case of thermal screening ($H_{\mathrm{sym}} = -\frac{1}{2}$), as expected.

In overall radius, GYSELA reproduces a value close to the theoretical prediction except in the region $0.1 < \rho < 0.5$. The main reasons for such a difference can be summarized as follows. First, poloidal asymmetries driven by turbulence can reduce the thermal screening effect through the geometric factor P_B in equation (23). Second, the term u in equation (15),
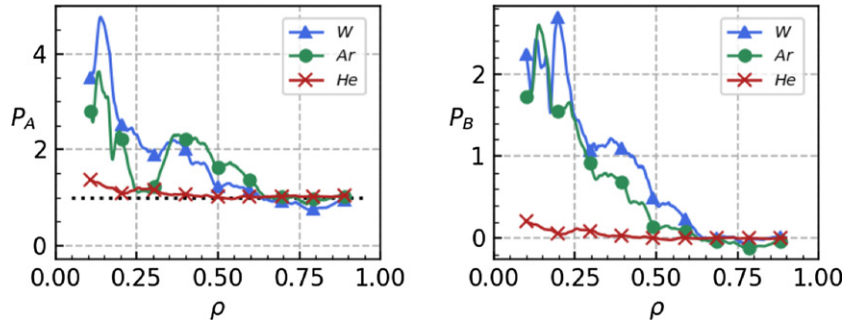
Figure 8. The radial profile of geometric factors P_A (left), P_B (right) without an external heating system.
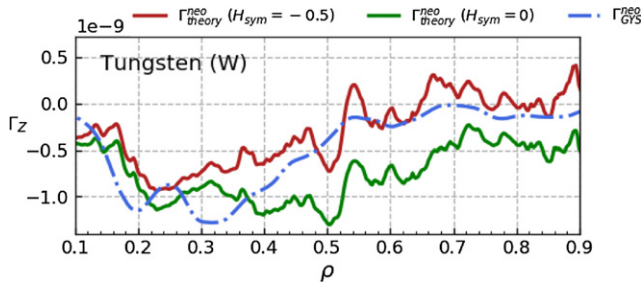

Figure 9. Neoclassical impurity flux of tungsten from the theoretical predictions of equations (14) and (15) with two different values of H_{sym}. With thermal screening, $H_{sym} = -\frac{1}{2}$ (red solid line) and without thermal screening, $H_{sym} = 0$ (green solid line). For comparison, the neoclassical impurity flux from GYSELA is also depicted (blue dashed line).

linked with the poloidal rotation of the main ions, is calculated for the neoclassical case only; thus, the value of k_{neo} in equation (16) differs from the neoclassical prediction ($k_{neo} \sim 1.17$) due to turbulence and it has been reported in [40] that the adjusted value of k_{neo} produces a better agreement.

4. Conclusions

In this work, numerical modelling of turbulent and neoclassical transport has been performed for various impurities—He, Ar and W—using the full-f gyrokinetic code GYSELA. Our results demonstrate that the main dominant particle flux and its direction sensitively depend on the type of impurity. Most of the light impurity (He) transport is due to turbulence, while heavy impurity (W) transport is dominated by neoclassical effects. Moreover, the two main driving terms for neoclassical flux—BP and PS fluxes—have been investigated. Our numerical simulations demonstrate that helium produces almost negligible BP and PS fluxes, compared to the other two impurities, due to its very low collisionality, while significant BP and PS fluxes are reproduced for argon and tungsten leading to inward accumulation.

In the absence of an external heating system, we have also verified that poloidal asymmetry driven by turbulence can modify the neoclassical particle flux, and its impact becomes more important in case of heavy impurities. Furthermore, these strong asymmetries for heavy impurities reduce the thermal screening factor which facilitates deleterious core accumulation. The neoclassical flux given by our analytical model is shown to be in good agreement with our numerical simulations and GYSELA reproduces a thermal screening factor close to that of the theoretical prediction $H_{sym} \simeq -\frac{1}{2}$.

Acknowledgments

Appendix A. Perpendicular flux and CGL pressure tensor

The perpendicular part of the particle flux consists of three different drift terms:

$$\mathbf{\Gamma}_\perp = N\mathbf{v}_E + N\langle\mathbf{v}_D\rangle - \nabla \times \left[N\left\langle\frac{\mu}{Ze}\mathbf{b}\right\rangle\right], \qquad (A.1)$$

where the magnetic drift consists of the curvature and ∇B drifts.

$$\mathbf{v}_{Ds} = \frac{m_s v_\parallel^2}{ZeB}\mathbf{b} \times \boldsymbol{\kappa} + \frac{\mu}{Ze}\mathbf{b} \times \nabla \ln B. \qquad (A.2)$$

Here, $\boldsymbol{\kappa} = (\mathbf{b} \cdot \nabla)\mathbf{b}$ is the magnetic curvature and $\boldsymbol{\kappa}$ can be expressed otherwise (appendix B).

$$\boldsymbol{\kappa} = \frac{\nabla_\perp B}{B} + \frac{\mu_0 \nabla \perp P}{B^2}. \qquad (A.3)$$

Applying an average of the distribution function ($\langle\ldots\rangle = \frac{1}{N}\int d^3\mathbf{v}\bar{F}_z\ldots$) over equation (A.2) leads to:

$$\mathbf{\Gamma}_{\perp D} = \frac{P_\parallel}{ZeB}\mathbf{b} \times \boldsymbol{\kappa} + \frac{P_\perp}{ZeB}\mathbf{b} \times \nabla \ln B, \qquad (A.4)$$

where we used the following relations

$$P_\parallel = \int d^3\boldsymbol{v} \bar{F} m v_\parallel^2$$
$$P_\perp = \int d^3\boldsymbol{v} \bar{F} \mu B \tag{A.5}$$

$$-\nabla \times \left[N \left\langle \frac{\mu}{Ze} \boldsymbol{b} \right\rangle \right] = \frac{\boldsymbol{B}}{ZeB^2} \times \nabla P_\perp - \frac{P_\perp}{ZeB} \boldsymbol{b}$$
$$\times \nabla \ln B - \frac{P_\perp}{ZeB} \nabla \times \boldsymbol{b} \tag{A.6}$$

using the following vector identities $\nabla(AB) = A\nabla B + B\nabla A$ and $\nabla\left(\frac{B}{A}\right) = \frac{A\nabla B - B\nabla A}{A^2}$.

Therefore, equation (A.1) can be recast as

$$\boldsymbol{\Gamma}_\perp = N\boldsymbol{v}_E + (P_\parallel - P_\perp)\frac{1}{ZeB}(\boldsymbol{b} \times \boldsymbol{\kappa}) + \frac{\boldsymbol{B}}{ZeB^2} \times \nabla P_\perp$$
$$= N\boldsymbol{v}_E + \frac{\boldsymbol{B}}{ZeB^2} \times \nabla \cdot \boldsymbol{\Pi}, \tag{A.7}$$

where we defined

$$\nabla \cdot \boldsymbol{\Pi} = \nabla P_\perp (P_\parallel - P_\perp)\boldsymbol{\kappa} + \left[(\boldsymbol{B} \cdot \nabla) \left(\frac{P_\parallel - P_\perp}{B} \right) \right] \boldsymbol{b}. \tag{A.8}$$

The radial particle flux can then be written as follows:

$$\langle \boldsymbol{\Gamma}_{\perp z} \cdot \nabla \psi \rangle_\psi = \left\langle \left[\frac{\boldsymbol{B}}{ZeB^2} \times (N_z e \nabla \phi + \nabla \cdot \boldsymbol{\Pi}) \right] \cdot \nabla \psi \right\rangle_\psi, \tag{A.9}$$

where the bracket $\langle \ldots \rangle$ corresponds to a flux surface average

$$\langle \mathcal{G} \rangle_\psi = \frac{\int \frac{d\theta\, d\varphi}{\boldsymbol{B} \cdot \nabla\theta} \mathcal{G}}{\int \frac{d\theta\, d\varphi}{\boldsymbol{B} \cdot \nabla\theta}}. \tag{A.10}$$

From the expression of the magnetic field $\boldsymbol{B} = I(\psi)\nabla\varphi + \nabla\varphi \times \nabla\psi$, one can find the useful relationship:

$$\frac{\boldsymbol{B}}{B^2} \times \nabla\psi = \frac{I}{B^2}\boldsymbol{B} - R^2\nabla\varphi. \tag{A.11}$$

In a steady state ($\partial_t = 0$) and with an axisymmetric system ($\partial_\varphi = 0$), equation (A.9) can be rewritten as

$$\langle \boldsymbol{\Gamma}_{\text{neo}} \cdot \nabla\psi \rangle_\psi = -\left\langle \frac{I}{ZeB^2}(N_z e \cdot \nabla\phi + \boldsymbol{B} \cdot \nabla \cdot \boldsymbol{\Pi}) \right\rangle_\psi. \tag{A.12}$$

It is still possible to further decompose equation (A.12) into two parts $\Gamma_{\text{neo}} = \Gamma_{\text{BP}} + \Gamma_{\text{PS}}$ using the identity [31]

$$\frac{1}{B} = \frac{1}{B} - \frac{B}{\langle B^2 \rangle_\psi} + \frac{B}{\langle B^2 \rangle_\psi}. \tag{A.13}$$

Finally, we obtain the impurity BP and PS fluxes, respectively.

$$\langle \boldsymbol{\Gamma}_{\text{BP}} \cdot \nabla\psi \rangle_\psi = -\frac{I}{Ze} \frac{\langle \boldsymbol{B} \cdot \nabla \cdot \boldsymbol{\Pi} \rangle_\psi}{\langle B^2 \rangle_\psi} \tag{A.14}$$

$$\langle \boldsymbol{\Gamma}_{\text{PS}} \cdot \nabla\psi \rangle_\psi = -\frac{I}{Ze} \left\langle (Ne\boldsymbol{b} \cdot \nabla\phi + \boldsymbol{b} \cdot \nabla \cdot \boldsymbol{\Pi}) \right.$$
$$\left. \times \left(\frac{1}{B} - \frac{B}{\langle B^2 \rangle_\psi} \right) \right\rangle_\psi. \tag{A.15}$$

Appendix B. Magnetic curvature

The magnetic curvature is defined as $\boldsymbol{\kappa} = (\mathbf{b} \cdot \nabla)\mathbf{b}$. Using the vectorial identity $A \times (\nabla \times B) = A \cdot \nabla B - (A \cdot \nabla)B$, we can rewrite the magnetic curvature:

$$\boldsymbol{\kappa} = (\mathbf{b} \cdot \nabla)\mathbf{b}$$
$$= -\mathbf{b} \times (\nabla \times \mathbf{b}) = -\mathbf{b} \times (\nabla \times \boldsymbol{B}/B)$$
$$= -\mathbf{b} \times \left(\nabla \left(\frac{1}{B} \right) \times \boldsymbol{B} \right) - \mathbf{b} \times (\nabla \times \boldsymbol{B})/B$$
$$= -\mathbf{b} \times (\mathbf{b} \times \nabla \ln B) + \mu_0 \boldsymbol{J} \times \boldsymbol{B}/B^2$$
$$= \frac{1}{B}[\nabla - \mathbf{b}(\mathbf{b} \cdot \nabla)]B + \mu_0 \boldsymbol{J} \times \boldsymbol{B}/B^2. \tag{B.1}$$

Defining $\nabla_\perp = \nabla - \mathbf{b}(\mathbf{b} \cdot \nabla) = -\mathbf{b} \times (\mathbf{b} \times \nabla)$ as the gradient perpendicular to $\boldsymbol{B}$, we can then rewrite the above equation as

$$\boldsymbol{\kappa} = \nabla_\perp \ln B + \frac{\mu_0 \boldsymbol{J} \times \boldsymbol{B}}{B^2} = \frac{\nabla_\perp B}{B} + \frac{\mu_0 \nabla_\perp P}{B^2}. \tag{B.2}$$

Appendix C. Parallel frictional force

In case of a heavy impurity in the trace limit, the frictional force $\mathcal{F}_{\parallel zi}$ can be written as a linear function of the parallel velocity $V_{\parallel s}$ and the parallel heat flux $q_{\parallel s}$ [24].

$$\mathcal{F}_{\parallel zi} = -N_z m_z \nu_{zi} \left[V_{\parallel z} - V_{\parallel i} - \frac{3}{5}\frac{1}{1 + x_{zi}^2}\frac{q_{\parallel z}}{N_z T_z} \right.$$
$$\left. + \frac{3}{5}\frac{1}{1 + x_{iz}^2}\frac{q_{\parallel i}}{N_i T_i} \right], \tag{C.1}$$

where $x_{ab} = v_{Tb}/v_{Ta}$.

It is worthwhile relating equation (10) with the frictional force $\mathcal{F}_{\parallel zi}$ to show how poloidal density asymmetry is linked with impurity flux (For a more complete derivation, see the appendix of [26].)

$$\mathcal{F}_{\parallel zi} = m_z \nu_{zi} \left[-N_z \frac{T_i}{eB}\frac{I}{L_\psi} + B(N_z u - K_z) \right], \tag{C.2}$$

where $1/L_\psi = 1/L_{\psi i} + 1/L_{\psi z}$ with $1/L_{\psi i} = \partial_\psi \ln P_i - \frac{3}{2}\partial_\psi \ln T_i$ and $1/L_{\psi z} = -\frac{1}{T_i Z N_z}\partial_\psi P_{\perp z}$ and u is the value related to the poloidal velocity of the main ions.

ORCID iDs

K. Lim https://orcid.org/0000-0002-0174-2300
X. Garbet https://orcid.org/0000-0001-5730-1259
Y. Sarazin https://orcid.org/0000-0003-2479-563X
E. Gravier https://orcid.org/0000-0002-8911-5546

References

[1] Pütterich T., Neu R., Dux R., Whiteford A.D., O'Mullane M.G. and Summers H.P. 2010 Calculation and experimental test of the cooling factor of tungsten *Nucl. Fusion* **50** 025012

[2] Maddison G.P. *et al* 2003 Impurity-seeded plasma experiments on JET *Nucl. Fusion* **43** 49

[3] Nave M.F.F. *et al* 2003 Role of sawtooth in avoiding impurity accumulation and maintaining good confinement in JET radiative mantle discharges *Nucl. Fusion* **43** 1204

[4] Hender T.C. *et al* 2016 The role of MHD in causing impurity peaking in JET hybrid plasmas *Nucl. Fusion* **56** 066002

[5] Loarte A. *et al* 2003 Characteristics of type I ELM energy and particle losses in existing devices and their extrapolation to ITER *Plasma Phys. Control. Fusion* **45** 1549

[6] Wade M.R., Burrell K.H., Leonard A.W., Osborne T.H. and Snyder P.B. 2005 Edge-localized-mode-induced transport of impurity density, energy, and momentum *Phys. Rev. Lett.* **94** 225001

[7] Casson F.J. *et al* 2013 Validation of gyrokinetic modelling of light impurity transport including rotation in ASDEX Upgrade *Nucl. Fusion* **53** 063026

[8] Bonanomi N., Mantica P., Giroud C., Angioni C., Manas P. and Menmuir S. 2018 Light impurity transport in JET ILW L-mode plasmas *Nucl. Fusion* **58** 036009

[9] Casson F.J. *et al* 2015 Theoretical description of heavy impurity transport and its application to the modelling of tungsten in JET and ASDEX upgrade *Plasma Phys. Control. Fusion* **57** 014031

[10] Angioni C. *et al* 2014 Tungsten transport in JET H-mode plasmas in hybrid scenario, experimental observations and modelling *Nucl. Fusion* **54** 083028

[11] Meyer H. *et al* 2019 Overview of physics studies on ASDEX Upgrade *Nucl. Fusion* **59** 112014

[12] Joffrin E. *et al* 2019 Overview of the JET preparation for deuterium–tritium operation with the ITER like-wall *Nucl. Fusion* **59** 112021

[13] Park H.K. *et al* 2019 Overview of KSTAR research progress and future plans toward ITER and K-DEMO *Nucl. Fusion* **59** 112020

[14] Lerche E. *et al* 2016 Optimization of ICRH for core impurity control in JET-ILW *Nucl. Fusion* **56** 036022

[15] Goniche M. *et al* 2017 Ion cyclotron resonance heating for tungsten control in various JET H-mode scenarios *Plasma Phys. Control. Fusion* **59** 055001

[16] Sertoli M., Angioni C. and Odstrcil T. 2017 Parametric dependencies of the experimental tungsten transport coefficients in ICRH and ECRH assisted ASDEX Upgrade H-modes *Phys. Plasmas* **24** 112503

[17] Kappatou A. *et al* 2019 Understanding helium transport: experimental and theoretical investigations of low-*Z* impurity transport at ASDEX Upgrade *Nucl. Fusion* **59** 056014

[18] Angioni C. and Helander P. 2014 Neoclassical transport of heavy impurities with poloidally asymmetric density distribution in tokamaks *Plasma Phys. Control. Fusion* **56** 124001

[19] Angioni C., Casson F.J., Mantica P., Pütterich T., Valisa M., Belli E.A., Bilato R., Giroud C. and Helander P. 2015 The impact of poloidal asymmetries on tungsten transport in the core of JET H-mode plasmas *Phys. Plasmas* **22** 055902

[20] Mollén A., Pusztai I., Fülöp T., Kazakov Y.O. and Moradi S. 2012 Effect of poloidal asymmetries on impurity peaking in tokamaks *Phys. Plasmas* **19** 052307

[21] Fulöp T. and Moradi S. 2012 Effect of poloidal asymmetry on the impurity density profile in tokamak plasmas *Phys. Plasmas* **18** 030703

[22] Maget P., Frank J., Nicolas T., Agullo O., Garbet X. and Lütjens H. 2020 Natural poloidal asymmetry and neoclassical transport of impurities in tokamak plasmas *Plasma Phys. Control. Fusion* **62** 025001

[23] Idomura Y., Obrejan K., Asahi Y. and Honda M. 2021 Dynamics of enhanced neoclassical particle transport of tracer impurity ions in ion temperature gradient driven turbulence *Phys. Plasmas* **28** 012501

[24] Hirshman S.P. and Sigmar D.J. 1981 Neoclassical transport of impurities in tokamak plasmas *Nucl. Fusion* **21** 1079

[25] Grandgirard V. *et al* 2016 A 5D gyrokinetic full-*f* global semi-Lagrangian code for flux-driven ion turbulence simulations *Comput. Phys. Commun.* **207** 35

[26] Donnel P. *et al* 2019 A multi-species collisional operator for full-*f* global gyrokinetics codes: numerical aspects and verification with the GYSELA code *Comput. Phys. Commun.* **234** 1

[27] Estève D. *et al* 2018 Self-consistent gyrokinetic modeling of neoclassical and turbulent impurity transport *Nucl. Fusion* **58** 036013

[28] Donnel P. *et al* 2019 Neoclassical impurity flux in presence of turbulent generated poloidal asymmetries and pressure anisotropy *Plasma Phys. Control. Fusion* **61** 044006

[29] Chew G.F., Goldberger M.L. and Low F.E. 1956 The Boltzmann equation and the one-fluid hydromagnetic equations in the absence of particle collisions *Proc. R. Soc.* A **236** 112

[30] Brizard A.J. and Hahm T.S. 2007 Foundations of nonlinear gyrokinetic theory *Rev. Mod. Phys.* **79** 421

[31] Helander P. and Sigmar D.J. 2005 *Collisional Transport in Magnetized Plasmas* (Cambridge: Cambridge University Press)

[32] Fülöp T. and Helander P. 1999 Nonlinear neoclassical transport in a rotating impure plasma with large gradients *Phys. Plasmas* **6** 3066

[33] Sarazin Y. *et al* 2011 Predictions on heat transport and plasma rotation from global gyrokinetic simulations *Nucl. Fusion* **51** 013023

[34] Manas P., Kappatou A., Angioni C. and McDermott R.M. 2020 Light impurity transport in tokamaks: on the impact of neutral beam fast ions *Nucl. Fusion* **60** 056005

[35] Casson F.J. *et al* 2020 Predictive multi-channel flux-driven modelling to optimise ICRH tungsten control and fusion performance in JET *Nucl. Fusion* **60** 066209

[36] Belli E.A. and Candy J. 2012 Full linearized Fokker–Planck collisions in neoclassical transport simulations *Plasma Phys. Control. Fusion* **54** 015015

[37] Houlberg W.A., Shaing K.C., Hirshman S.P. and Zarnstorff M.C. 1997 Bootstrap current and neoclassical transport in tokamaks of arbitrary collisionality and aspect ratio *Phys. Plasmas* **4** 3230

[38] Romanelli M. and Ottaviani M. 1998 Effects of density asymmetries on heavy impurity transport in a rotating tokamak plasma *Plasma Phys. Control. Fusion* **40** 1767

[39] Donnel P., Garbet X., Sarazin Y., Asahi Y., Wilczynski F., Caschera E., Dif-Pradalier G., Ghendrih P. and Gillot C. 2019 Turbulent generation of poloidal asymmetries of the electric potential in a tokamak *Plasma Phys. Control. Fusion* **61** 014003

[40] Breton S. *et al* 2018 High *Z* neoclassical transport: application and limitation of analytical formulae for modelling JET experimental parameters *Phys. Plasmas* **25** 012303